Influence of solidification structures on radiation-induced swelling in an additively-manufactured austenitic stainless steel

G. Meric de Bellefon [a, *], K.M. Bertsch [a], M.R. Chancey [b], Y.Q. Wang [b], D.J. Thoma [a]

[a] Department of Materials Science and Engineering, University of Wisconsin, Madison, WI, 53706, USA
[b] Materials Science and Technology Division, Los Alamos National Laboratory, Los Alamos, NM, 87545, USA

HIGHLIGHTS

- Radiation-induced swelling observed in additively-manufactured (AM) 316 L stainless steel.
- Swelling twice as large in as-fabricated state compared to post-processed states.
- Swelling promoted by AM-induced dislocations.
- Swelling inhibited near AM-induced precipitates.

GRAPHICAL ABSTRACT
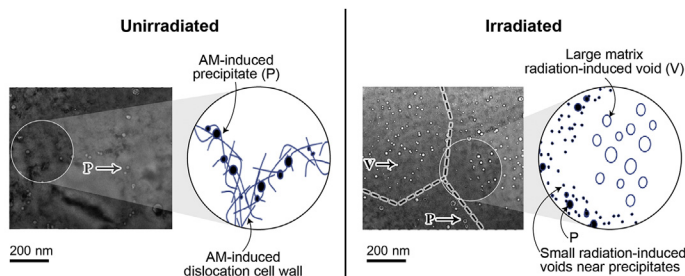
ARTICLE INFO

ABSTRACT

Metal additive manufacturing offers potential advantages for producing structural materials, such as austenitic stainless steels, in nuclear power systems. However, the microstructure developed during metal additive processing is notably different from the one developed in conventional processing, and the influence of the microstructural differences on performance in radiation environments has not been fully quantified. Using heavy ion irradiation and transmission electron microscopy, the radiation-induced swelling response of a laser powder-bed fusion-manufactured austenitic stainless steel was investigated at high doses. The influence of solidification-induced dislocation and precipitate structures was studied by comparing the radiation-induced swelling response of a 316 L stainless steel in three microstructural states: as-fabricated, solution annealed, and fully recrystallized. Void swelling was approximately twice as pronounced in the as-fabricated state compared to post-processed states. In the framework of the rate theory for radiation effects, the higher swelling in the as-fabricated state can be explained by the strong sink bias for interstitial point defects exerted by the intermediate density of pre-existing dislocations. Void swelling was inhibited in the vicinity of pre-existing precipitates, but the density of precipitates in the as-fabricated material was not enough to compensate for the increase in swelling caused by dislocations.

1. Introduction

Metal additive manufacturing (AM) technologies offer the ability to rethink the design of components without the constraints of conventional fabrication methods. Specifically, AM permits the fabrication of complex geometries in a one-step process [1]. However, the engineering application of AM materials requires the ability to maintain mechanical properties and degradation resistance compared to conventional materials. In metal AM methods such as laser powder-bed fusion (LPBF), the extreme processing

---

* Corresponding author.
E-mail address: mericdebelle@wisc.edu (G. Meric de Bellefon).

conditions create unique systems compared to those observed in conventional processing routes such as metal casting and welding, due to orders of magnitude larger solidification rates and thermal stresses [1]. A physical understanding of structure-property relationships is needed, requiring new qualification and certification efforts to ensure reproducible performance [2]. Metal AM methods offer opportunities to design novel microstructures leading to materials properties that can be equivalent to conventionally-made materials, and in some cases superior. For example, recent studies have shown that metal AM of austenitic stainless steel (SS) can allow breaking the strength-ductility trade-off [3] or superior corrosion resistance [4,5] compared to conventional SS.

The potential benefits of using AM to build structural materials for nuclear power applications [6,7] warrants studying the radiation response of AM materials. Austenitic stainless steels are used in all current nuclear reactors and are candidate materials for many advanced reactor designs [8,9] because of their good mechanical properties and corrosion resistance, including at high temperatures. However, their radiation resistance can be poor, especially at intermediate temperatures (400−600 °C) where they are susceptible to void swelling under neutron irradiation [10−12]. The evolution of swelling with dose usually occurs in two regimes: a low-swelling-rate incubation regime (swelling rate of less than 0.01%/ dpa) followed by a high-swelling-rate regime (swelling rates from 0.4 to 1%/dpa for irradiation temperatures between 400 and 600 °C [13−15]). Several strategies have been designed to reduce swelling or lengthen the incubation regime in SS by introducing a high density of sinks for point defects such as precipitates and cold-work-induced dislocations structures [16−20], grain boundaries [21], or twin boundaries [22]. Metal AM SS may offer enhanced radiation resistance due to the production of very heterogeneous microstructures [3] with potential sinks for point defects such as dendritic segregation boundaries, sub-granular dislocation cell walls, and oxide precipitates [23]. A recent study reported promising radiation resistance of metal AM 316 L SS after 2.5-dpa proton irradiation at 360 °C [24].

In the present work, the response of LPBF-manufactured 316 L SS to ion irradiation at the doses of 50 and 100 dpa is reported. Ion irradiation was used as a surrogate for neutron irradiation. Three microstructural states - as fabricated, solution annealed, and fully recrystallized - from the same 316 L stainless steel composition were studied to clarify the role of solidification-induced precipitates and dislocation structures on radiation-induced swelling. The solution annealing treatment was intended to partially recover the sub-granular solidification structures and is commonly used as a stress relief treatment in AM steels. The fully recrystallized state was intended to create a control microstructural state in which sub-granular solidification structures have been fully removed from the microstructure.

2. Experimental

2.1. Test materials

The test material was EOS 316 L SS with composition shown in Table 1. The composition was measured with combustion infrared detection (C and S), inert gas fusion (O and N), and direct current plasma emission spectroscopy (all other elements). Rectangular parallelepiped samples of approximately $3 \times 10 \times 50$ mm were manufactured in an EOS M290 LPBF system using the EOS recommended process parameters: laser power of 195 W, laser speed of 1083 mm/s, hatch spacing of 90 μm, and layer thickness of 20 μm. The starting feedstock powder had an average particle diameter of 40 μm. Three samples were prepared from the printed parallelepiped samples: 1) an *as-fabricated sample*, prepared by cutting a

section parallel to the build direction (see schematic in Fig. 1) and no post-processing treatment; 2) a *solution-annealed sample*, cut in the same fashion as the as-fabricated sample and subsequently annealed at 1050 °C for 1 h in argon atmosphere followed by a water quench; 3) a *fully-recrystallized sample*, cut in the same fashion and subsequently homogenized at 1200 °C for 4 h, cold-rolled to 90% thickness reduction, and annealed at 1050 °C for 1 h in argon atmosphere followed by a water quench. Prior to irradiation, all three samples were mechanically ground to a 1200 grit surface finish, and electropolished with a standard A2 electrolyte (ethanol, perchloric acid) at −15 °C for 10 min to remove approximately 200 μm of matter from the surface, thereby removing the majority of defects induced by mechanical polishing [25].

2.2. Irradiation experiments

The samples were irradiated on the electropolished surfaces with 3.5-MeV Fe^{2+} ions at 500 °C at a flux of approximately 3.4×10^{12} ions/cm²s. Significant swelling is expected under these irradiation conditions [21,22]. During the first set of irradiations, the samples were irradiated at a fluence of 5×10^{16} ions/cm². The damage and injected Fe^{2+} ion profiles were simulated with the Stopping and Range of Ions in Matter code [26] using the "Kinchin-Pease" option and the threshold displacement energy of 40 eV for all the target elements. Simulations calculated peak damage depth of approximately 50 dpa at 1 μm, with damage extending to 1.5 μm below the surface. The corresponding simulated profile is shown in Fig. 2. A second set of irradiations was conducted to study the swelling evolution with dose: the as-fabricated and fully recrystallized samples were irradiated to a higher fluence of 1×10^{17} ions/cm² (i.e., 100 dpa). A defocused ion beam was used for all irradiations to better emulate neutron irradiation [27].

2.3. Microstructure characterization techniques

Electron backscatter diffraction (EBSD) mapping of the electropolished surfaces of the samples was performed in an FEI Helios G4 UX Extreme High Resolution Field Emission Scanning Electron Microscope equipped with an EDAX Hikari Super EBSD camera and TEAM EBSD data collection software. An accelerating voltage of 30 kV, current of 26 nA, and step size of 190 nm were used for each sample. Cross-sectional specimens for transmission electron microscopy (TEM) were extracted from the irradiated surfaces (see schematic in Fig. 1) with a focused ion beam (FIB) in a Zeiss Auriga using 30 kV Ga⁺ ions for machining followed by 5 kV Ga + ions for polishing. Conventional TEM imaging of voids was performed in an FEI Tecnai TF-30 equipped with a Schottky field-emission electron gun operated at 300 kV. Scanning TEM (STEM) analysis was performed in an FEI Titan aberration-correct STEM equipped with a Schottky field-emission electron gun operated at 200 kV and a high-angle annular dark field detector (HAADF).

3. Results

3.1. Microstructural analysis

The electro-polished surfaces of the samples showing the grain morphologies are shown in the EBSD maps of Fig. 3. The maps are colorized according to the crystal orientation that is aligned with the build direction (vertical direction) and boundaries with local misorientations higher than 5° are shown in black. The as-fabricated sample exhibits columnar grains and a ⟨001⟩ texture in the build direction. In the solution-annealed sample, grains are more equiaxed and less textured. In the fully-recrystallized sample, the grain structure is typical of a wrought stainless steel with large

Table 1
Composition of the test EOS 316 L SS.

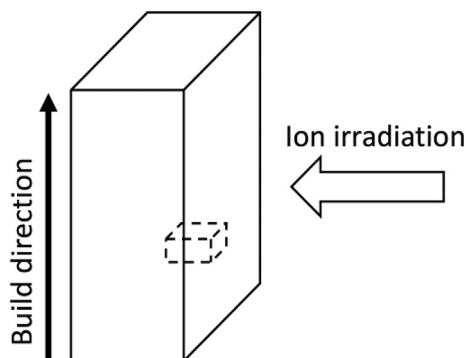| Element	Fe	Ni	Cr	Mo	Si	Mn	C	N	Cu	P	O
wt%	Balance	13.94	18.39	2.86	0.30	1.47	0.004	0.065	0.0022	0.017	0.043

Fig. 1. Schematic showing the build direction of the AM 316 L test part, the surface exposed to irradiation, and the orientation of cross-sectional TEM specimens extracted after irradiation (dashed box).
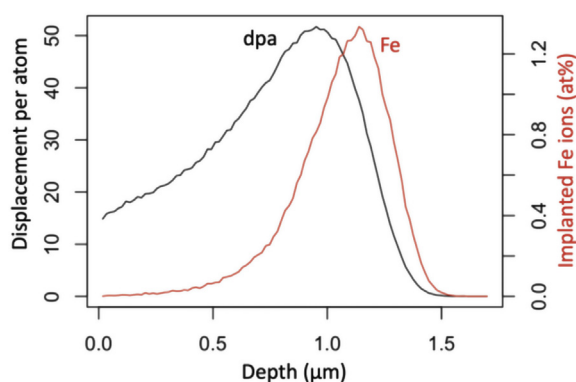

Fig. 2. Damage and implanted Fe^{2+} ions profiles calculated with Monte-Carlo-based SRIM tool [26] for a fluence of 5×10^{16} ions/cm^2.

Fig. 3. EBSD maps of the surface of (a) the as-fabricated sample, (b) the solution-annealed sample, and (c) the fully-recrystallized sample, colorized according to the crystal orientation aligned with the build direction (vertical direction). The boundaries with local misorientation higher than 5° are shown in black.

equiaxed grains and annealing twins. An effective boundary density was estimated by measuring the length per unit area of boundaries with local misorientations higher than 5°. The effective boundary density was measured to be approximately 0.20–0.30 μm^{-1} for all samples. It should be noted that these boundaries may not only consist of classical planar grain boundaries, but likely also include dense dislocation cell boundaries separating regions with relative misorientations greater than 5°.

STEM HAADF micrographs of the microstructures in the cross-sectional TEM specimens after 50 dpa irradiation are shown in Fig. 4, in which the region below the top irradiated surface is representative of the pre-irradiation microstructure. The irradiated region has a higher defect content and extends from the surface of the specimen to approximately 1.5 μm deep in all three samples, as indicated by the double-ended arrows, consistent with the SRIM simulation (Fig. 2). Outside of the irradiated zone, the preexisting microstructure in the as-fabricated sample, shown in Fig. 4a, exhibits the sub-granular cellular structure typical of LPBF-manufactured 316 L SS [3,7]. Cell walls consist of tangled dislocations, appearing with lighter contrast, and fine precipitates with diameters on the order of tens of nm, appearing with darker contrast in Fig. 4a–c. Previous work indicated that the precipitates
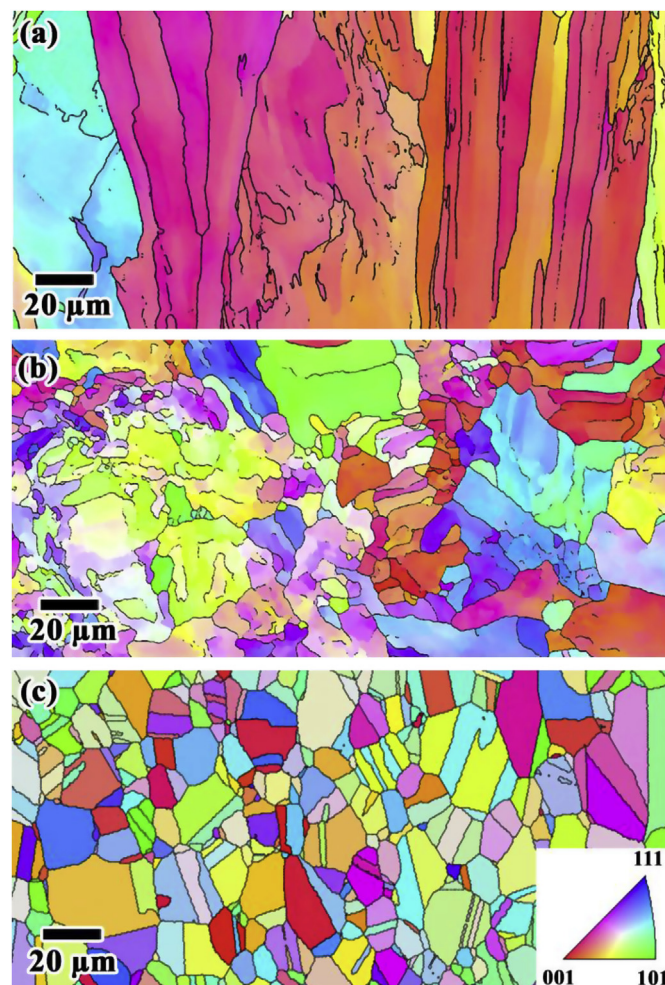
were oxides with varying amounts of Si, Mn, and Cr [3], which was confirmed in the present work with STEM energy dispersive spectroscopy. In the solution-annealed sample (Fig. 4b), the un-irradiated zone exhibits a lower density of dislocations than in the as-fabricated sample and a lower density of precipitates that are larger on average than in the as-fabricated state. In the fully-recrystallized sample (Fig. 4c), the un-irradiated zone exhibits no dislocations and even larger, sparser precipitates. Examples of dislocation walls and precipitates are indicated by arrows and labeled "D" and "P", respectively, in Fig. 4. In the irradiated region of the as-fabricated specimen shown in Fig. 4a, some defined dislocation cell walls are present, but are less visible amidst the background of irradiation-induced defects than they are in the un-irradiated region. The density and average diameter of precipitates, as measured from the un-irradiated zone of the cross-sectional TEM specimens are approximately 4×10^{20} m^{-3} and 15 nm respectively in the as-fabricated sample, approximately
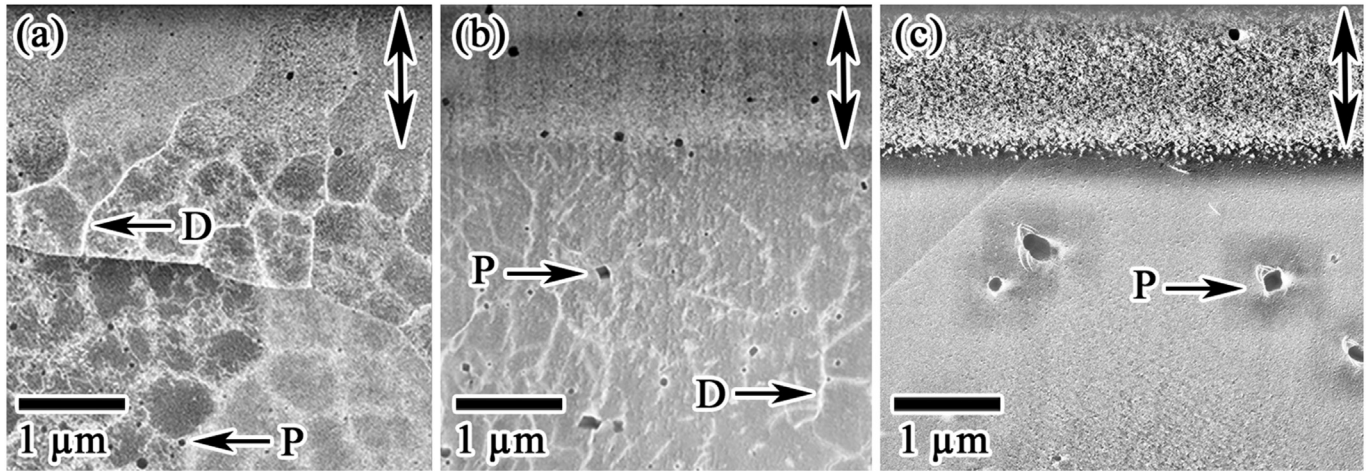
Fig. 4. STEM HAADF micrographs of the cross-sectional TEM specimens from (a) the as-fabricated 316 L sample, (b) the solution-annealed 316 L sample, and (c) the fully-recrystallized sample, after 3.5 MeV Fe^{2+} irradiation at 500 °C to a fluence of 5×10^{16} cm^{-2} (approximately 50 dpa). D: dislocation wall. P: precipitate. The double-ended arrows indicate the irradiation damage region.

0.3×10^{20} m^{-3} and 38 nm respectively in the solution-annealed sample, and approximately 0.03×10^{20} m^{-3} and 1.5×10^{2} nm respectively in the fully-recrystallized sample.

3.2. Void swelling

Voids were imaged in a TEM using the through-focus technique
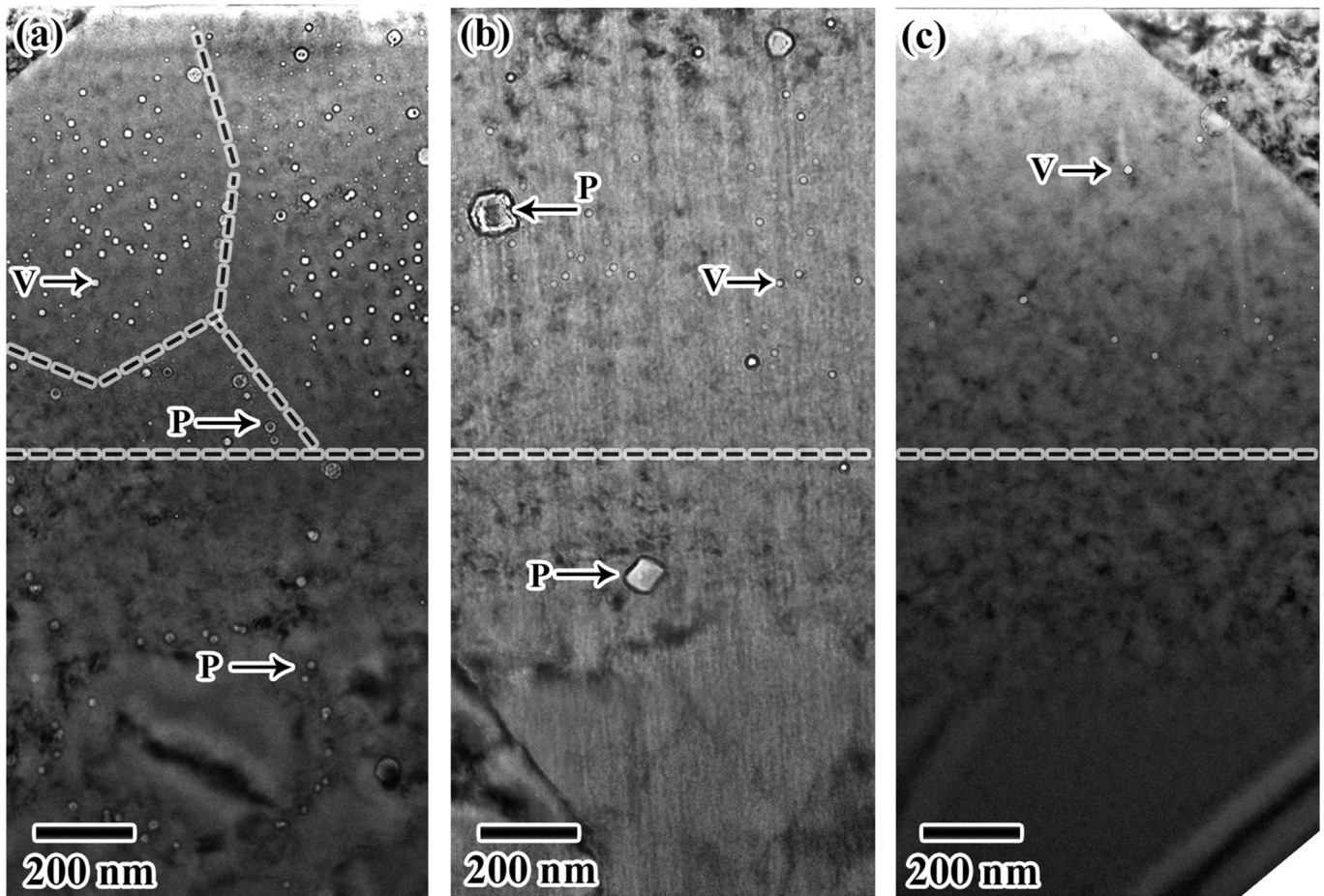

Fig. 5. TEM micrographs of the microstructure immediately beneath the surface after irradiation in under-focused condition of the cross-sectional specimens from (a) the as-fabricated 316 L sample, (b) the solution-annealed 316 L sample, and (c) the fully recrystallized 316 L sample after irradiation to 5×10^{16} cm^{-2} (approximately 50 dpa). The dashed line indicates the bottom of the region considered in quantifying void swelling (approximately 900 nm depth, which is not the entire 1.5 μm-deep damage layer). Voids and precipitates show a similar contrast. Voids are present in the irradiated region, while precipitates are present in both the irradiated and the unirradiated region − examples are indicated (V: void. P: precipitate). In (a), the dashed lines indicate the likely location of pre-existing cell walls.

[28]: voids have a dark Fresnel fringe in the under-focused condition and a bright Fresnel fringe in the over-focused condition. Better void contrast is usually obtained when no single beam is strongly diffracting [28], which reduces background contrast for dislocations and crystallographic defects. Under-focused images of the TEM cross-sectional specimens irradiated to 50 dpa are shown in Fig. 5. Voids appear as regions of bright contrast surrounded by dark Fresnel fringes, while precipitates generally, but not always, appear as regions of varied contrast surrounded by dark Fresnel fringes. Examples of voids and precipitates are indicated by arrows labeled "V" and "P", respectively, in Fig. 5. Since voids and precipitates can exhibit similar contrast characteristics, it was necessary to differentiate between the two for statistical analysis of voids. To estimate the void size distribution in the irradiated region, the precipitate size distribution in the un-irradiated region (region greater than 1.5 μm below the surface in Fig. 5) was estimated, then subtracted from the combined void and precipitate size distribution in the irradiated region. Void diameters were counted and measured in the region extending from the top surface to 900 nm depth in all samples (above the dashed horizontal line in Fig. 5). Note that this depth is less than the approximately 1.5 μm depth of the entire damage layer - it has been shown that ion irradiation leads to void swelling suppression in the deeper region of the damage (between approximately 1 μm and 1.5 μm deep), where a high amount of interstitials are injected [29,30]. Void swelling was estimated by approximating voids as spheres and computing the corresponding total volume occupied by voids. The thicknesses of cross-sectional TEM specimens were measured using the Electron Energy-Loss Spectrometry (EELS) method [31] and SEM imaging of specimens end-on, and were used to estimate the volume of the analyzed areas. In all samples, zones approximately 50–100 nm near precipitate/matrix interfaces tend to contain a higher density of smaller voids compared to elsewhere in the irradiated zone; examples are shown in Fig. 6. In the as-fabricated sample, regions

with pre-existing precipitates surrounded by smaller voids and denuded of large voids seem to correspond to pre-existing cell walls, as indicated by the dashed line in Fig. 5a.

Void diameters, void densities, and void swelling amounts are summarized in Table 2. The 100 dpa irradiation was only conducted on the as-fabricated and fully-recrystallized samples, since the fully-recrystallized and solution-annealed samples behaved very similarly at 50 dpa. The evolutions of both the void size distribution and void swelling with dose for the as-fabricated and fully-recrystallized samples are shown in Fig. 7. Swelling amounts and void densities are more pronounced in the as-fabricated sample, compared to either of the post-processed samples. In all samples, the dominant contributor to the overall swelling is the large void population.

4. Discussion

4.1. Influence of pre-existing dislocations on void swelling

The driving force for void formation is a supersaturation of vacancies that originates with the creation of point defects from irradiation-induced displacement cascades [32]. Unbiased point defect sinks such as grain boundaries can lower the matrix content of both interstitials and vacancies. Densities of boundaries with greater than $5°$ local misorientation (approximately $0.20–0.30\ \mu m^{-1}$ for the all samples) are expected to be too low to significantly influence swelling - grain boundary density effects on swelling typically only occur for sub-micron grain sizes [21,22,33–37], which is equivalent to boundary densities higher than approximately $2\ \mu m^{-1}$ [38]. Dislocations are biased sinks for interstitials and can increase the supersaturation of vacancies, leading to void swelling [19,39]. In the rate theory for radiation effects, the swelling rate is driven by the sink strength ratio, which is the ratio of dislocation sink strength to void sink strength [32,40]:
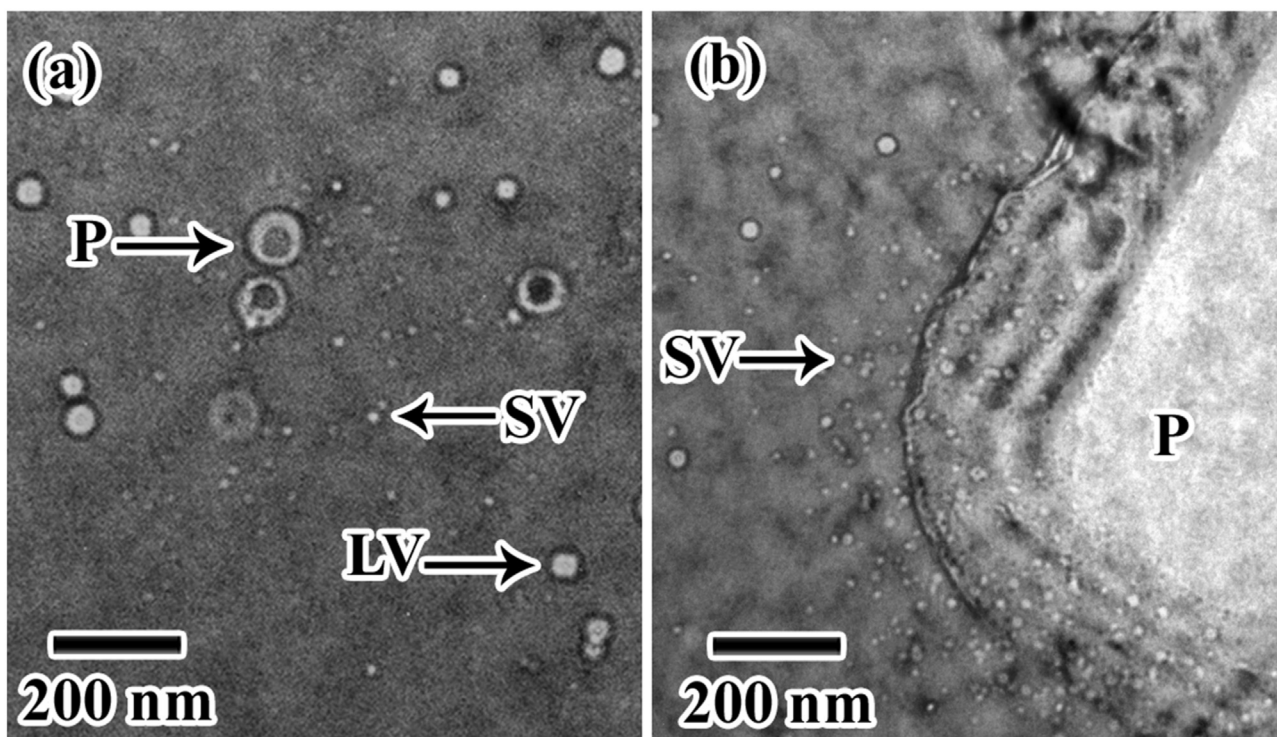

Fig. 6. Example of higher densities of smaller voids near pre-existing precipitates in (a) as-fabricated 316 L and (b) fully recrystallized 316 L samples after irradiation to $5 \times 10^{16}\ cm^{-2}$ (approximately 50 dpa). P: Precipitates; SV: Small voids; LV: Large voids.

Table 2
Void swelling after 3.5 MeV Fe^{2+} irradiation at 500 °C in the three materials.

	Dose dpa	Mean void diameter (nm)	Void density (10^{21} m^{-3})	Void swelling (%)
As-fabricated 316 SS	50	9.6 ± 1	2.7 ± 0.7	0.26 ± 0.05
	100	7.6 ± 1	4.0 ± 1.0	0.33 ± 0.07
Solution-annealed 316 SS	50	17 ± 1	0.48 ± 0.1	0.14 ± 0.03
Fully recrystallized 316 SS	50	15 ± 1	0.46 ± 0.1	0.12 ± 0.03
	100	15 ± 1	0.60 ± 0.1	0.15 ± 0.03

swelling rates are small at low and high sink strength ratios, and high at intermediate sink strength ratios close to unity, where the dislocation sink bias exerts the greatest influence on swelling rate. The dislocation sink strength is proportional to the dislocation density, and the void sink strength is proportional to the void number density and the void radius. The pre-existing dislocation density in the as-fabricated sample does not appear to limit swelling. Indeed, lower swelling occurred in the solution-annealed and fully-recrystallized samples, where the dislocation densities were significantly lower. Dislocation densities in AM and conventional cold-worked 304 SS were recently measured with neutron diffraction [41]; it was found that the dislocation density in as-fabricated AM 304 SS was one order of magnitude lower than in conventional 304 SS strained to 32%. Conventionally-fabricated SS cold-worked by tens of percent are known to swell less than annealed conventional SS [19,32] because of the high sink strength ratios after cold work. The intermediate dislocation density in AM as-fabricated SS creates an intermediate sink strength ratios closer to unity, which in turns leads to higher swelling rates than in the solution-annealed and fully-recrystallized SS.

4.2. Influence of pre-existing precipitates on void swelling

The 50 to 100 nm-wide zone denuded of large voids and exhibiting a high density of smaller voids is seen near the precipitate/matrix interfaces in all samples. This suggests that precipitate/matrix interfaces in all samples promote the formation of a high density of small voids in their vicinity. The formation of smaller voids near precipitates can be driven by the presence of oxygen. Oxygen is known to assist void formation by reducing the void-matrix surface energy [17,42–44]. Oxygen can be made available in the vicinity of the oxygen-rich precipitates through thermal spike-induced intermixing [45]. The sink strength of spherical voids increases rapidly with decreasing void radius [32,39]. Formation of a large number of smaller voids in the vicinity of precipitates, rather than a few larger voids, increases the local void sink strength, and thus decrease the sink strength ratio. As detailed above, the sink strength ratio is likely close to unity in the as-fabricated material, leading to higher swelling by a factor of two. A decrease in sink strength ratio near precipitates would therefore lead to lower swelling near precipitates in this sample, which is consistent with the observations (see dashed lines in Fig. 5a). Since this effect was confined to a zone of approximately 50 to 100-nm near the precipitate/matrix interface, while sub-granular cells are approximately 500 nm in diameter, the local swelling inhibition by precipitates is not expected to counterbalance the overall swelling enhancement caused by dislocations in the as-fabricated material. The roles of AM-induced dislocations and precipitates is summarized in Fig. 8.

4.3. Implications for the use of metal additive manufacturing in nuclear power systems

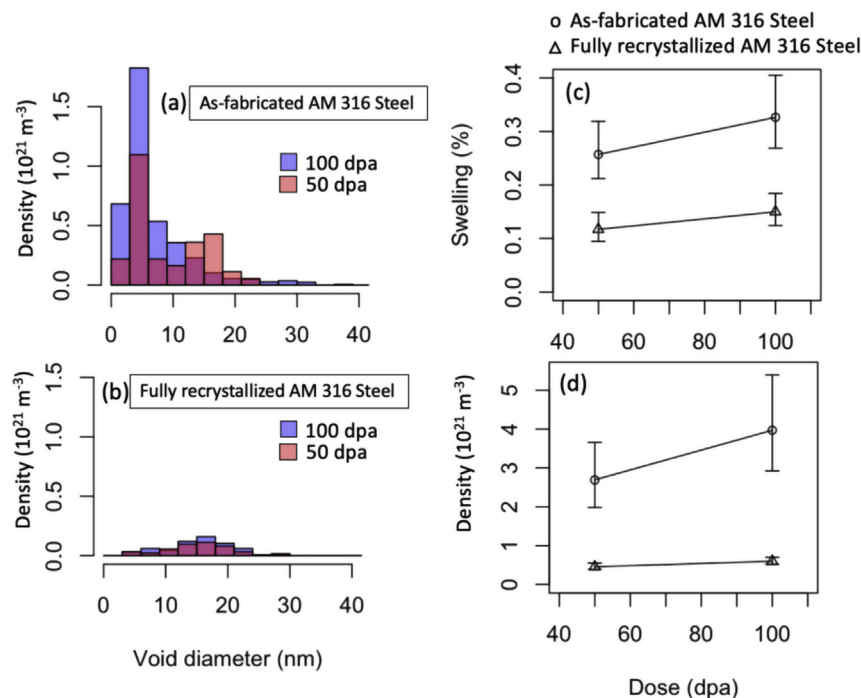In the studied AM process, the use of the default processing

Fig. 7. Evolution of void size distributions with dose in (a) AM as-fabricated 316 L and (b) AM fully recrystallized 316 L SS. Swelling (c) and void density (d) evolutions with dose in as-fabricated and recrystallized states.
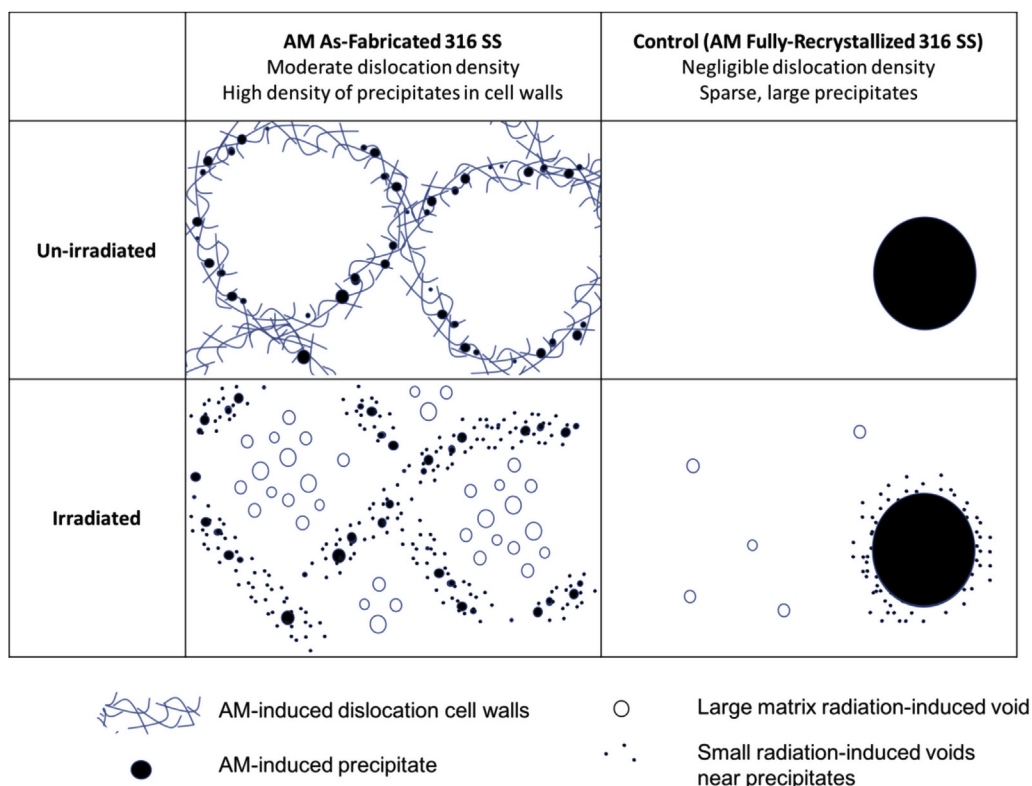
Fig. 8. Summary of influence of AM-induced precipitates and dislocations on void swelling.

parameters for 316 L is not desirable for radiation tolerance of components under ion irradiation since the as-fabricated microstructure appears to promote swelling. Strategies could be designed to increase densities of dislocations and precipitates in the as-fabricated state by modifying AM process parameters (e.g., Ref. [47]). These strategies could lead to swelling-resistant microstructures equivalent or superior to conventional cold-worked stainless steels due to the presence of additional precipitates that can inhibit swelling. In this study, ion irradiation is used here as a surrogate for neutron irradiation [46]. Further ion irradiation or neutron irradiation testing would be warranted to confirm that the observations are applicable to the use of AM components in nuclear power systems.

5. Conclusions

The present work studied the radiation-induced swelling response at high doses of a 316 L austenitic stainless steel additively manufactured with a laser powder-bed fusion system. Three material states were considered: as-fabricated, solution-annealed, and fully-recrystallized. Samples were irradiated with heavy ions to study the influence of solidification-induced cellular structures comprising dislocations and precipitates. Void swelling at 50 dpa and 100 dpa was approximately twice as high in the as-fabricated state, as compared to the fully-recrystallized state. The solution-annealed and fully-recrystallized materials exhibited similar void swelling at 50 dpa. The intermediate density of pre-existing dislocations in the as-fabricated state is suggested to have promoted swelling compared to post-processed states, which can be rationalized by the rate theory of radiation effects. Void swelling was inhibited in the vicinity of pre-existing precipitates, but the density of precipitates in the as-fabricated state was not enough to compensate for the increase in swelling caused by the intermediate

dislocation density. Strategies to increase densities of dislocations and precipitates during additive manufacturing of stainless steel could lead to enhanced radiation-induced swelling resistance.

References

[1] W.E. Frazier, Metal additive manufacturing: a review, J. Mater. Eng. Perform. 23 (6) (2014) 1917—1928.
[2] B.C. Salzbrenner, et al., High-throughput stochastic tensile performance of additively manufactured stainless steel, J. Mater. Process. Technol. 241 (2017) 1—12.
[3] Y.M. Wang, et al., Additively manufactured hierarchical stainless steels with high strength and ductility, Nat. Mater. 17 (1) (2018) 63—70.
[4] Q. Chao, et al., On the enhanced corrosion resistance of a selective laser melted austenitic stainless steel, Scripta Mater. 141 (2017) 94—98.
[5] M.J.K. Lodhi, K.M. Deen, W. Haider, Corrosion behavior of additively manufactured 316L stainless steel in acidic media, Mater. 2 (June) (2018) 111—121.
[6] Y. Zhong, et al., Additive manufacturing of ITER first wall panel parts by two approaches: selective laser melting and electron beam melting, Fusion Eng. Des. 116 (2017) 24—33.
[7] Y. Zhong, L. Liu, S. Wikman, D. Cui, Z. Shen, Intragranular cellular segregation network structure strengthening 316L stainless steel prepared by selective

laser melting, J. Nucl. Mater. 470 (2016) 170–178.

[8] T.R. Allen, et al., Materials challenges for generation IV nuclear energy systems, Nucl. Technol. 162 (3) (2008) 342–357.

[9] S.J. Zinkle, L.L. Snead, Designing radiation resistance in materials for fusion energy, Annu. Rev. Mater. Res. 44 (1) (2014) 241–267.

[10] C. Cawthorne, E.J. Fulton, Voids in irradiated stainless steel, Nature 216 (5115) (Nov. 1967) 575–576.

[11] F.A. Garner, D.S. Gelles, Neutron-induced swelling of commercial alloys at very high exposures, Eff. Radiat. Mater. 14th Int. Sym- posium (Volume II) 2 (May) (1990) 673–683.

[12] S. Hamada, P.J. Maziasz, M.P. Tanaka, M. Suzuki, A. Hishinuma, Temperature dependence of swelling in type 316 stainless steel irradiated in HFIR, J. Nucl. Mater. 155–157 (PART 2) (1988) 838–844.

[13] F.A. Garner, Recent insights on the swelling and creep of irradiated austenitic alloys, J. Nucl. Mater. 122 (1–3) (May 1984) 459–471.

[14] F.A. Garner, H.R. Brager, The influence of Mo, Si, P, C, Ti, Cr, Zr and various trace elements on the neutron-induced swelling of AISI 316 stainless steel, J. Nucl. Mater. 155–157 (PART 2) (1988) 833–837.

[15] R.E. Stoller, P.J. Maziasz, A.F. Rowcliffe, M.P. Tanaka, Swelling behavior of austenitic stainless steels in a spectrally tailored reactor experiment: implications for near-term fusion machines, J. Nucl. Mater. 155–157 (PART 2) (1988) 1328–1334.

[16] E.E. Bloom, J.O. Stiegler, A comparison of irradiation-induced swelling and void formation in two austenitic stainless steels, J. Nucl. Mater. 35 (2) (1970) 244–246.

[17] E.H. Lee, L.K. Mansur, Relationships between phase stability and void swelling in Fe-Cr-Ni alloys during irradiation, Metall. Trans. A, Phys. Metall. Mater. Sci. 23 (7) (1992) 1977–1986.

[18] B.J. Makenas, S.A. Chastain, B.C. Gneiting, "Dimensional Changes in Fftf Austenitic Cladding and Ducts," LMR: A Decade of LMR Progress and Promise, ANS Winter Meeting, 1990.

[19] F.A. Garner, Radiation Damage in Austenitic Steels, first ed., vol. 4, Elsevier Inc., 2012.

[20] S.J. Zinkle, P.J. Maziasz, R.E. Stoller, Dose dependence of the microstructural evolution in neutron-irradiated austenitic stainless steel, J. Nucl. Mater. 206 (2–3) (1993) 266–286.

[21] C. Sun, et al., Superior radiation-resistant nanoengineered austenitic 304L stainless steel for applications in extreme radiation environments, Sci. Rep. 5 (2015) 7801.

[22] G. Meric de Bellefon, I.M. Robertson, T.R.R. Allen, J.-C.C. van Duysen, K. Sridharan, Radiation-resistant nanotwinned austenitic stainless steel, Scripta Mater. 159 (Jan. 2019) 123–127.

[23] J. Megusar, O.K. Harling, N.J. Grant, Potential for using rapid solidification for improved irradiation performance in the fusion environment, J. Nucl. Mater. 104 (Jan. 1981) 961–965.

[24] M. Song, M. Wang, X. Lou, R.B. Rebak, G.S. Was, Radiation damage and irradiation-assisted stress corrosion cracking of additively manufactured 316L stainless steel, J. Nucl. Mater. 513 (2019) 33–44.

[25] D. Aliya, B.L. Adams, D. Alman, ASM Handbook Volume 9 Metallography and Microstructures, ASM International, 2018.

[26] J.F. Ziegler, M.D. Ziegler, J.P. Biersack, SRIM - the stopping and range of ions in matter (2010), Nucl. Instrum. Methods Phys. Res. Sect. B Beam Interact. Mater.

Atoms 268 (11–12) (2010) 1818–1823.

[27] J.G. Gigax, et al., The influence of ion beam rastering on the swelling of self-ion irradiated pure iron at 450 °C, J. Nucl. Mater. 465 (2015) 343–348.

[28] M.L. Jenkins, M.A. Kirk, Characterization of Radiation Damage by Transmission Electron Microscopy, 2001.

[29] F.A. Garner, Impact of the injected interstitial on the correlation of charged particle and neutron-induced radiation damage, J. Nucl. Mater. 117 (C) (1983) 177–197.

[30] L. Shao, Effect of defect imbalance on void swelling distributions produced in pure iron irradiated with 3.5 MeV self-ions, J. Nucl. Mater. 453 (1–3) (2014) 176–181.

[31] D.B. Williams, C.B. Carter, The Transmission Electron Microscope, 2009.

[32] Gary S. Was, Fundamentals of Radiation Materials Science, Springer Berlin Heidelberg, Berlin, Heidelberg, 2007.

[33] O. El-Atwani, J.A. Hinks, G. Greaves, J.P. Allain, S.A. Maloy, Grain size threshold for enhanced irradiation resistance in nanocrystalline and ultrafine tungsten, Mater. Res. Lett. 5 (5) (2017) 343–349.

[34] B. Radiguet, A. Etienne, P. Pareige, X. Sauvage, R. Valiev, Irradiation behavior of nanostructured 316 austenitic stainless steel, J. Mater. Sci. 43 (23–24) (2008) 7338–7343.

[35] B.N. Singh, A.J.E. Foreman, Calculated grain size-dependent vacancy supersaturation and its effect on void formation, Philos. Mag. A 29 (4) (1974) 847–857.

[36] M. Hatakeyama, H. Watanabe, M. Akiba, N. Yoshida, Low void swelling in dispersion strengthened copper alloys under single-ion irradiation, J. Nucl. Mater. 307–311 (1 SUPPL) (2002) 444–449.

[37] B.N. Singh, S.J. Zinkle, Defect accumulation in pure fcc metals in the transient regime: a review, J. Nucl. Mater. 206 (2–3) (1993) 212–229.

[38] J.C. Russ, R.T. Dehoff, Practical Stereology, Springer Science & Business Media, 2000.

[39] G.R. Odette, M.J. Alinger, B.D. Wirth, Recent developments in irradiation-resistant steels, Annu. Rev. Mater. Res. 38 (1) (2008) 471–503.

[40] L.K. Mansur, Theory and experimental background on dimensional changes in irradiated alloys, J. Nucl. Mater. 216 (C) (1994) 97–123.

[41] D.W. Brown, et al., In situ neutron diffraction study of the influence of microstructure on the mechanical response of additively manufactured 304L stainless steel, Metall. Mater. Trans. A 48 (12) (2017) 6055–6069.

[42] S.J. Zinkle, E.H. Lee, Effect of oxygen on vacancy cluster morphology in metals, Metall. Trans. A 21 (5) (1990) 1037–1051.

[43] S.J. Zinkle, F.A. Garner, Effect of initial oxygen content on the void swelling behavior of fast neutron irradiated copper, J. Nucl. Mater. 329–333 (1-3 PART B) (2004) 938–941.

[44] E.H. Lee, L.K. Mansur, Fe-15Ni-13Cr austenitic stainless steels for fission and fusion reactor applications. I. Effects of minor alloying elements on precipitate phases in melt products and implication in alloy fabrication, J. Nucl. Mater. 278 (1) (2000) 1–10.

[45] I.J. Beyerlein, M.J. Demkowicz, A. Misra, B.P. Uberuaga, Defect-interface interactions, Prog. Mater. Sci. 74 (2015) 125–210.

[46] G.S. Was, et al., Emulation of reactor irradiation damage using ion beams, Scripta Mater. 88 (2014) 33–36.

[47] L. Liu, et al., Dislocation network in additive manufactured steel breaks strength–ductility trade-off, Mater. Today 21 (4) (May 2018) 354–361.